nature communications

Article

https://doi.org/10.1038/s41467-025-64481-0

Ultra-high entropy rare earth phosphate against environmental corrosion

Received: 21 October 2024

Accepted: 15 September 2025

Published online: 27 October 2025

Check for updates

Fuhao Cheng [1,2,3], Donald B. Dingwell [1,4,5] & Wenjia Song [1,2,3,5]

Environmental particulate deposits are the most severe factor causing high-temperature corrosion failure in advanced structural materials. Yet, the primary mechanisms of molten material corrosion under extreme conditions remain unclear, hindering the development and improvement of new crucial corrosion-resistant materials. "Ultra-high entropy" rare earth orthophosphates (REPOs) are one such promising class of materials. Here, we investigate the high-temperature structural state and properties of a wide range of substitutions involving 15 (La, Ce, Pr, Nd, Sm, Eu, Gd, Tb, Dy, Ho, Er, Tm, Yb, Lu and Y) rare earth elements in phosphates. Using stepwise stoichiometric compositional design, we aim to systematize our understanding of the corrosion resistance behavior of these complexes RE phosphates. We observe that high compositional complexity slows the reaction kinetics. Increasing rare-earth ionic radius, correlates positively with the chemical inertness of the synthesized material. This is overlain by phase state considerations whereby single-phase compositions exhibit the highest corrosion resistance. In summary, we infer that 1) the grade of complexity of rare earth mixtures; 2) the proportions of the individual rare earths and 3) the phase state of solid solution stoichiometries are the key factors in determining the corrosion resistance of these complex phosphate materials.

Advanced structural ceramics are inorganic non-metallic materials with exceptional properties, often heralding technological breakthroughs[1–3]. Designed to withstand extreme mechanical and thermal loads while maintaining outstanding stability, these materials are crucial for aerospace propulsion and thermal protection systems[4]. Ceramic materials are currently processed into core turbine components for aircraft as well as spacecraft (including Lunar and Martian mission applications) as (1) thermal[5,6]/environmental barrier coatings[7] (T/EBCs), (2) ceramic matrix composites (CMCs)[8], and (3) high-temperature structures for spacecraft[9]. The extreme conditions encountered in aerospace missions severely restrict the range of viable materials[4,10]. The emergence of new material design approaches (e.g., high-throughput computing[11,12]) and paradigms (e.g., artificial intelligence[13,14]) are leading to a surge in proposed new compositions with diverse characteristics to tackle these extreme environments. Despite this, one of the major challenges associated with these materials - the deleterious effects of their interactions with environmental particles[15] - have been largely neglected.

Particulate matter suspended in Earth's atmosphere, includes sand, dust, and volcanic ash, is often investigated using simplified CMAS (Calcium-Magnesium-Alumino-Silicates)[16–18] analogs. But volcanic ash is a multiphase assemblage of glass, several crystalline phases (as phenocrysts, microlites, and nanolites), and salt coatings. Such materials melt readily in high-temperature environments, subsequently adhering to components and causing sustained damage[19–21]. In the planetary mission context, reports indicate that soil compositions

[1]GEOLAB, Hangzhou International Innovation Institute, Beihang University, Hangzhou, China. [2]Tianmushan Laboratory, Beihang Unviersity, Hangzhou, China. [3]School of Materials Science and Engineering, Beihang University, Beijing, China. [4]Department of Earth and Environmental Sciences, Ludwig-Maximilians-Universität (LMU) Munich, Munich, Germany. [5]International Research Institute for Multidisciplinary Science, Beihang University, Beijing, China.
e-mail: songwj@buaa.edu.cn

on Lunar and Martian surfaces are also composed of very fine-grained, highly reduced, mixtures of glasses, metals, and rock-forming minerals, thus presenting even more technical challenges for foreseeable human exploration activities[22,23].

To counter corrosion risk, previous research has provided a plethora of new candidate materials[24–26]. Of these, rare earth phosphates have emerged in recent years as a class of high-temperature protective materials and are considered one of the candidate materials for T/EBCs due to their excellent stability and corrosion resistance[27–29]. At the design level, compositional optimization targets a balance of overall performance[30–32].

Here, we synthesized a class of so-called "ultra-high entropy" rare earth orthophosphates, of the following stoichiometries MPO_4, $(M_{75}X_{25})PO_4$, $(M_{50}X_{50})PO_4$, $(M_{25}X_{75})PO_4$, XPO_4, where M = La, Ce, Pr, Nd, Sm, Eu, Gd in equal amounts and X = Tb, Dy, Ho, Er, Tm, Yb, Lu, Y in equal amounts. MPO_4, $(M_{75}X_{25})PO_4$, and XPO_4 yield single phases of monazite and xenotime structures, respectively. $(M_{50}X_{50})PO_4$ and $(M_{25}X_{75})PO_4$ yield two-phase mixtures of monazite + xenotime structures. Thus, the phase diagram for this multicomponent binary system displays a solvus in which stoichiometries $(M_{50}X_{50})PO_4$ and $(M_{25}X_{75})PO_4$ reside in the two-phase field. Below, we refer to all of these binary mixtures as MXPOs.

While all MXPOs exhibit excellent high-temperature stability and corrosion resistance, our investigation reveals that the M/X ratio significantly qualitatively influences the corrosion behavior of the samples. Through a comprehensive analysis of factors, including infiltration mechanisms, reaction products, and deposit typologies, we have systematically elucidated the protective mechanisms. We provide empirical data supporting the development of novel rare earth phosphates as well as a fundamental framework for optimizing their corrosion resistance properties.

Results and discussion

Design concept and crystal structure

High-entropy materials often contain multiple ions in equivalent lattice sites, and their structure tends to change with composition. To elucidate the influence of element types on the crystal structure and properties of high-entropy phosphates, we divided the 15 elements into two groups, following the observation that lanthanide rare-earth orthophosphates exhibit two different crystal structures depending on the ionic radius (Fig. 1a and Supplementary Fig. 5).

Using gadolinium as the "boundary element", we categorized the elements into two groups: (i) The M group, consisting of 7 elements (La, Ce, Pr, Nd, Sm, Eu, Gd) with larger ionic radii, which tend to form the monazite structure; (ii) and the X group, comprising 8 elements (Tb, Dy, Ho, Er, Tm, Yb, Sc, Y, Lu) with smaller ionic radii, which tend to form the xenotime structure (Fig. 1b and Supplementary Fig. 18). As noted above the monazite structure (monoclinic, $P2_1/n$) accommodates larger rare earth ions compared with the xenotime structure (tetragonal, $I4_1/amd$). This distorts the polyhedra in the unit cell, resulting in lower structural symmetry. Consequently, the inherent characteristics of the monazite structure differ from those of the more ordered xenotime structure crystals.

We have determined the phase state of a series of MXPOs designed by modulating the M/X element ratio. Five groups of ceramic powders with systematically varied stoichiometric REE ratios were selected for characterization (Fig. 1c, Supplementary Fig. 6 and Supplementary Table 1–3). Regardless of how the element proportions changed, the results indicate that no independent diffraction peaks corresponding to starting components were observed, suggesting that all samples had fully formed solid solutions (Fig. 1d and Supplementary Fig. 19). As an example, $M_{75}X_{25}PO$ formed a single M phase despite the fact that it contains 25% of X group elements (Supplementary Fig. 11).

As the M/X ratio gradually decreases, the crystal structure of the samples exhibits a transition from single M phase to the coexistence of multiple phases, and finally to single X phase. We note here that as where M group elements were present, MXPOs did not form a single X phase, indicating that larger radius ions have poor solubility in the X phase lattice. Furthermore, the lattice constants of the X phase indicate that $M_{25}X_{75}PO$ is slightly smaller than XPO (Supplementary Fig. 15). This can be understood from the solid solution behavior of simple rare earth phosphates: Elements in group X with relatively larger radii exhibit a stronger propensity to enter the M structure, resulting in the retention of smaller elements within group X. This phenomenon leads to a reduction in the lattice constant of the X phase composed of these remaining elements. Evidently, within ultra-high entropy phosphates, while the M structure can accommodate a certain amount of small-radius X ions, the X structure has limited capacity to dissolve larger M ions.

Descriptor for phase formation tendency

Having verified the crystal structures and microscopic morphologies of all ultra-high entropy MXPOs, it becomes evident that as the M/X ratio decreases, the crystal structures of the samples exhibit a transition whose systematic nature enables us to refine certain characteristics to describe this phenomenon. Inspired by the structural patterns of low-entropy $REPO_4$ that vary with ionic radii (Supplementary Table 4 and Supplementary Fig. 16), we introduce a phase formation tendency factor C, which incorporates information on elemental proportions and ionic radii, to describe the solid solution rules of complex compositional phosphates:

$$C = \log_{10}\left(\frac{\sum_1^i (R_M \cdot \alpha_M) - R}{-\sum_1^j (R_X \cdot \alpha_X) - R} \cdot \frac{n}{1-n}\right) (1)$$

Where $\sum_1^i (R_M \cdot \alpha_M) - R$ and $-\sum_1^j (R_X \cdot \alpha_X) - R$ respectively consider the ionic radii and proportions of each component in the M and X groups. These are subtracted from $R = 1.052$ ($R_{Gd3+} = 1.053$) to describe the 'tendency' of the component to form M/X phases. In addition, the $n/1-n$ describe the total proportions of M and X elements, respectively.

Based on the magnitude of the C value, the phase space is divided into three regions. We compared the structures of various complex phosphates, all of which exhibited similar trends, yet differences in specific behaviors were observed (Fig. 1e). Firstly, near the multi-phase boundary (e.g., C = 0.2), medium and low-entropy orthophosphates show a minimal amount of X phase, corresponding to the small-radius ion content just exceeding the solid solution limit. However, in MXPOs, the X phase is already quite prominent. This indicates that the average value related to ionic radii and content cannot accurately represent the M-X solid solution behavior. Secondly, for the X single-phase region, it can only form in MXPOs when M elements are absent, probably attributed to the fact that in MXPO systems, regardless of how small the content of M group elements is, there are still elements with very large ionic radii that cannot adapt to the X lattice. These two differences will promote the broadening of the actual multi-phase region of ultra-high entropy orthophosphates under the measure of the *C*-value. Therefore, a more conservative strategy should be adopted when designing high-entropy single-phase compositions.

Crystallography and morphology

The variation in elemental proportions gives rise to diverse phase compositions. Raman spectroscopy results reveal that the multiphase MXPOs exhibit the lowest peak intensity and maximum peak width for the symmetric stretching vibration of P-O bonds (Fig. 2a and Supplementary Fig. 7), indicating a high degree of disorder in the P-O tetrahedra. Moreover, the blue shift observed in the spectra indicates that as X group ions progressively substitute for the large-radius M ions, then the consequent reduction in lattice constant leads to

https://doi.org/10.1038/s41467-025-64481-0

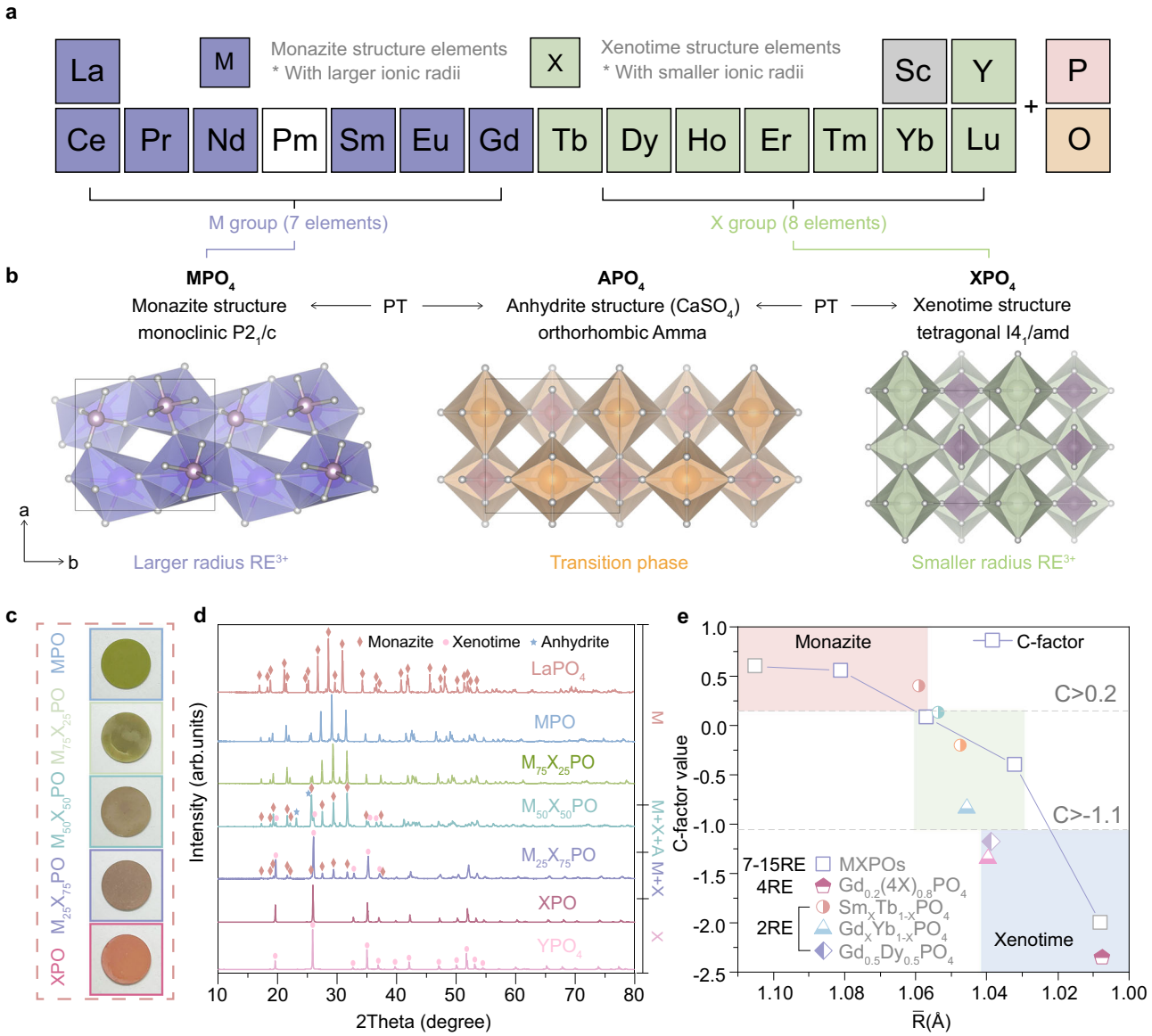

Fig. 1 | Design and structural characterization of ultra-high entropy phosphates MXPOs. a Periodic table highlighting all the elements used for the synthesis of MXPOs, color-coded according to the ground state crystal structure of the respective elemental phosphates. The cations considered for use here encompass almost the vast majority of lanthanide rare earth elements. **b** The phosphates of the selected rare earth cations have different crystal structures. Those with larger ionic radii tend to form monazite structures, and vice versa tend to form xenotime structures. In addition, an anhydrite structure exists as a transition state where the two phases transform into each other (PT = Phase transition). **c** Optical digital photographs of the prepared MXPOs ceramic pellets and (**d**) the corresponding XRD crystal structure analysis diagrams. (for further detail see Supplementary Note. 2 and 3). **e** Descriptor for rare earth phosphates of complex composition. The phase state and C values of complex-simple composition phosphates currently synthesized using the M + X hybrid model was collected. where MPO and XPO calculations of *C*-values are meaningless and are schematized using gray dots. Data beyond the square points are from the composition and structure of high, medium, and low entropy value phosphates[29,40,49,50]. (for further data see Supplementary Table. 4).

compression of the P-O tetrahedra. Generally, where M and X phases coexist, the polyhedra exhibit a higher degree of distortion and deformation.

From the XPS analysis results (Fig. 2b and Supplementary Figs. 8, 9), rare earth elements are all uniformly present in the + 3-valence state. For anions, the high-resolution O*1s* spectrum shows only lattice oxygen and adsorbed oxygen peaks, with no significant oxygen vacancies observed.

To evaluate the influence of elemental proportions on the morphology of MXPOs, observations and analyses were conducted at multiple scales. At the macroscopic scale (Fig. 2c, d and Supplementary Figs. 10–14), regardless of variations in elemental proportions, the samples exhibit no significant morphological changes, with each group demonstrating low porosity, high density, and excellent uniformity in elemental distribution. Microscale analysis was conducted using TEM, taking $M_{75}X_{25}PO$ and XPO as examples. The observed interplanar spacings were found to correspond with the database values for M and X phases (Fig. 2e–g). In addition, the positions of the selected area electron diffraction (SAED) rings provided further confirmation of the MXPOs structure. Finally, analysis of nanoscale particles using HAADF imaging revealed that MXPOs maintain excellent uniformity in elemental distribution even at this scale.

High-temperature properties of MXPOs

Composition directly influences the phase state of these high-entropy materials, whereby the limits of solid solution are a function of

https://doi.org/10.1038/s41467-025-64481-0

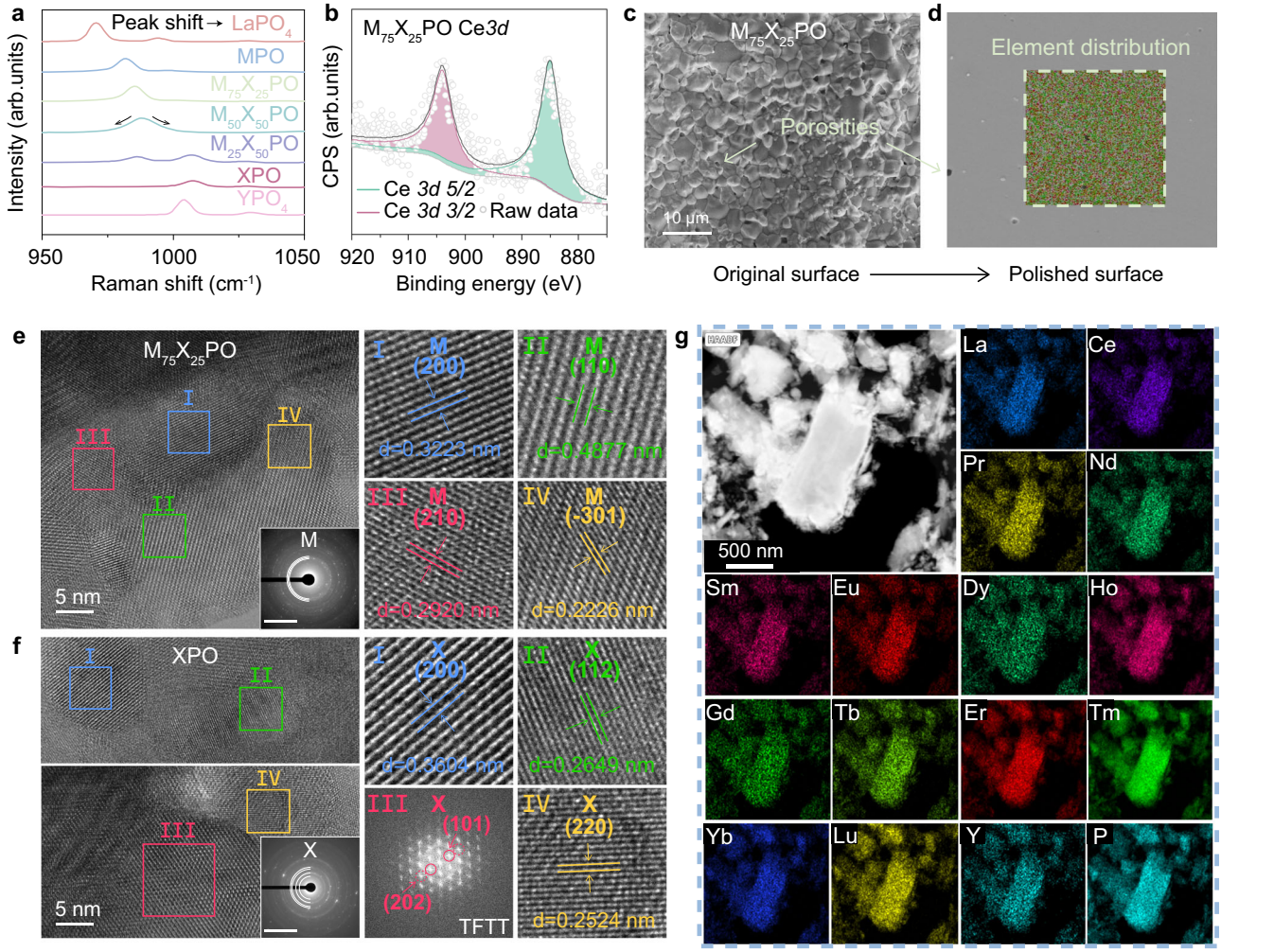

Fig. 2 | Crystallographic properties and microscopic morphology of MXPOs. **a** The Raman spectra of MXPOs reflect the distortion of the P-O polyhedral. Intercepts of 950–1050 cm^{-1} were made to observe changes in the symmetric stretching vibrational peaks representing P-O bonds. **b** Taking the element Ce as an example, the XPS spectra show that the rare earth ions in the MXPOs are all in the + 3-valence state. **c**, **d** The sintered surface and elemental distribution of $M_{75}X_{25}PO$ and its flat surface after polishing make it easy to distinguish between porosity and impurities. (for further detail see Supplementary Note. 4). **e**, **f** High-resolution lattice fringing images of $M_{75}X_{25}PO$ and XPO in as well as the corresponding diffraction images of the SAED modes (inset figures). The plane spacing calculated by the Fourier transform of the image and the position of the polycrystalline rings obtained by diffraction can be corresponded to the standard data representing the M and X phases. SAED scale bar, 5 nm^{-1}. **g** The particles of $M_{75}X_{25}PO$ in which the distribution of the elements.

temperature. Some systems stabilized by entropy values form a single phase during heating and separate upon cooling. The original MXPOs powders, containing hydrous reagents (carrying stoichiometric, structurally-bound, water) form homogeneous solid solutions after annealing (Supplementary Fig. 17). Above 1600 °C, intermediate phases emerge in the M/X phases. These phases maintain their high-temperature structure after low-temperature annealing, indicating that their ultra-high entropy values may thermodynamically stabilize these structures at lower temperatures (Supplementary Note. 2).

To investigate thoroughly the high-temperature stability of MXPOs, we conducted a comprehensive analysis, dividing the temperature range into three segments. At temperatures below 1200 °C, no additional diffraction peaks due to phase transitions or decomposition were observed with temperature increase in MXPOs (Fig. 3a, b and Supplementary Figs. 21, 22). We note that a shift of the entire peak group was observed, attributed to the expansion of the lattice with temperature. Subsequently, in the medium temperature range (T < 1500 °C), both heat flow and weight remained highly stable, with no endothermic/exothermic reactions occurring. Lastly, samples subjected to cyclic thermal shock exceeding 1600 °C maintained their original crystal structure, with no macroscopic signs of melting. Thus, MXPOs demonstrate outstanding stability throughout the entire temperature range of use.

Thermal protection materials generally require a substantial thermal insulation capability. Here, laser thermal conductivity data determined for the MXPOs negatively correlate with temperature increase due to phonon scattering (Fig. 3e–g). However, at high temperatures, some samples show an increase rather than a decrease of thermal conductivity with temperature, which we attribute to the enhancement of radiative heat transfer in certain lattices as described by the Stefan-Boltzmann law[33,34]. We note as well that samples with an M structure begin to exhibit an increase in thermal conductivity at relatively lower temperatures, which is attributed to a substantial increase in their specific heat capacity at ca. 700 °C. Further, as the M/X ratio shifts, the thermal conductivity trend shows an initial decrease followed by an increase, particularly for $M_{50}X_{50}PO$.

The monazite structure, due to its higher disorder, has a lower thermal conductivity, and the presence of low-density intermediate phases further enhances its thermal insulation capacity (~ 1.1–6 $W{\cdot}m^{-1}{\cdot}K^{-1}$). XPO, containing no M elements and possessing a pure X structure, typically exhibits high thermal conductivity (> 10 $W{\cdot}m^{-1}{\cdot}K^{-1}$) in single rare-earth phosphates[28]. The ultra-high-

https://doi.org/10.1038/s41467-025-64481-0

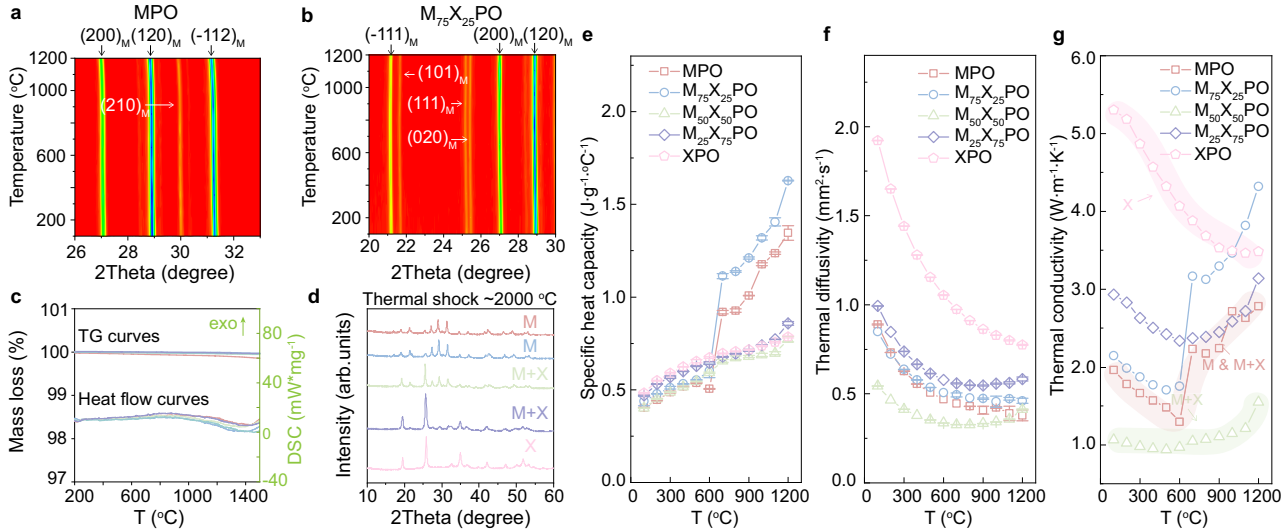

Fig. 3 | Phase stability and high-temperature thermal shielding performance tests of MXPOs. a, **b** In situ temperature-dependent changes in XRD diffraction peaks of specific crystal planes of MXPOs. The peak ranges with higher intensity corresponding to the M/X structure are included. **c** Dynamic thermal analysis of MXPOs, including weight changes with high temperature and heat flow changes representing heat exchange. **d** Crystal structure of MXPOs after treatment with thermal vibration cycling at ~2000 °C. **e** The specific heat capacity of MXPOs obtained through experiments, (**f**) the thermal diffusivity at corresponding temperatures, and (**g**) the calculated thermal conductivity. Samples with different M/X ratios exhibited differentiated values. Error bars represent the standard deviations of the results of three repeated trials. The shaded area is used to emphasize the trend of the thermal conductivity of MXPOs varying with temperature. (for further detail see Supplementary Note. 6).

entropy design produces a theoretically disordered distribution of different rare-earth ions at equivalent cation sites, resulting in local positional distortions driven by differences in ionic size and mass[35,36]. Thermal transport in defect-bearing materials depends on phonon propagation, and these lattice distortions introduce additional phonon scattering[34,37], thereby reducing thermal conductivity. From a macroscopic perspective, the thermal insulation capability of MXPOs is notably improved compared with that of low-entropy phosphates.

Thermal expansion behavior is critical for potential T/EBC applications. As the concentration of X-group ions increases, the thermal expansion coefficient of MXPOs gradually decreases, and depending on the predominant phase, they may be well-matched to distinct substrates (Supplementary Fig. 23). Thus, by tuning the proportions of ions with different radii within a high- or ultra-high-entropy framework to control the coefficient of thermal expansion, MXPOs gain enhanced versatility for practical applications.

Corrosion behavior of MXPOs with artificial CMAS

Despite their inherent stability, advanced high-entropy materials must face environmental corrosion in high-temperature settings. Thus, a detailed investigation of their interaction with environmental deposits is required. We selected a synthetic CMAS glass with relatively simple composition (in mol.%, 33CaO-9MgO-13$AlO_{1.5}$-45SiO_2) as the source of corrosive attack on MXPOs. The vertical cross-sections of samples after 10 h of reaction at 1300 °C revealed several corrosion products resulting from CMAS-MXPOs interactions, with corrosion depth increasing with the M/X ratio (Fig. 4a–c). The color-coded regions in the figure represent compact and dense reaction product layers, whose thicknesses were calculated separately. Notably, XPO presented an anomaly in this trend, with two superimposed thin dense layers isolating the CMAS melt from the ceramic, implying reduced corrosion space and reaction opportunities. Furthermore, the multiphase $M_{25}X_{75}PO$ formed a grain boundary penetration layer encapsulating the reaction products beneath the dense layer, while simultaneously exhibiting the thickest dense layer, yielding inferior corrosion resistance.

Further examination of the reaction cross-section reveals that the CMAS-MXPOs interaction produces crystalline products of several morphologies, exhibiting a certain regularity in their spatial distribution (Fig. 4a, e). For example, dense, dark-contrast products adhere closely to the ceramic surface, above which smaller ellipsoidal and larger needle-like crystals are more widely distributed. These reaction products partition the reaction space into three layers, with the loosely packed crystals macroscopically dispersed within the melt, and relative ineffectiveness in impeding CMAS penetration. We cannot, however, fully exclude the possibility that the needle-like crystals have formed on the quench. Regardless, we infer that the third layer of dense products adjacent to the ceramic is the primary contributor to impeding corrosion.

The results of compositional analysis by SEM-EDS indicate that the loosely packed/suspended crystals are rich in REs, while P and Ca are the primary constituents of the dense layer (Fig. 4e–g and Supplementary Fig. 26). Based on stoichiometry, the interfacial products consist of apatite (Ap) generated by reaction between CMAS melt and orthophosphate. The chemistry of this apatite possibly expressed by the general structural formula of $Ca_{2+x}RE_{8-x}(PO_4)_x(SiO_4)_{6-x}O_2$[27,38,39]. The densely packed P-rich phase also contains minor amounts of REEs and Mg, which may correspond to $Ca_8MgRE(PO_4)_7$[40]. Further, REs and P from MXPOs exhibit distinct dissolution fates such that P content is higher near the MXPO ceramic, while REs are primarily enriched in the region of loosely suspended Ap crystals. In the XRD analysis of the MXPOs-CMAS mixed system, relatively distinct apatite diffraction peaks were identified, and clear diffraction patterns (belonging to the P63/m space group) were observed in the SAED results (Supplementary Figs. 27–29). These results confirm our speculation regarding the types of reaction products.

Comparing the Ap morphologies with different M/X ratios reveals that larger-radius rare earth elements precipitate two types of Ap at the interface: acicular low RE Ap with lower rare earth content and more equant Ap with higher rare earth content. Focusing solely on acicular Ap, an increase in quantity and crystal size is observed as the M/X ratio rises. Analysis of elemental composition in different Ap morphologies indicates that among M-group elements, Ce, Nd, Sm, Eu, and Gd exhibit higher dissolution rates, suggesting enhanced reactivity (Fig. 4h, i). Conversely, for X-group elements, only crystals with varying

https://doi.org/10.1038/s41467-025-64481-0

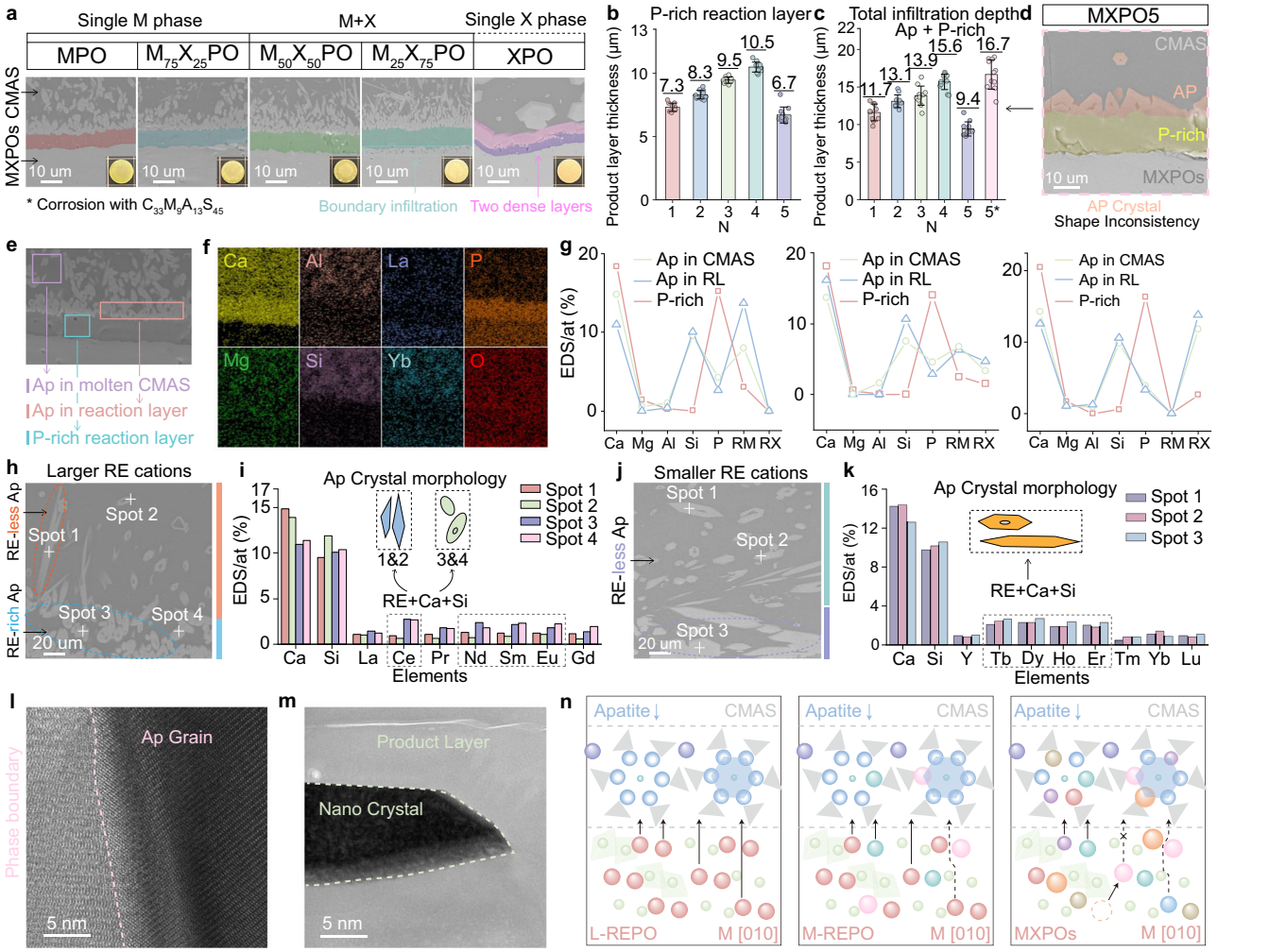

Fig. 4 | High-temperature reaction behavior of MXPOs with artificial CMAS. **a** Cross-sectional morphology of MXPOs after corrosion with CMAS at 1300 °C for 10 h. The color-marked area represents the dense reaction product layer. The inset figures represent the top morphology of the MXPOs ceramic after being loaded with CMAS and corroded. **b**, **c** Thickness of the dense layer as well as the overall product layer thickness. The number on the line is the average value of thickness. **d** Alternative form of corrosion in XPO, which is distributed in lower quantities. **e**, **f** Spatial distribution of $M_{75}X_{25}PO$-CMAS reaction products, as well as morphological differences, were analyzed, and corresponding elemental mappings. **g** Elemental composition of the reaction products in MPO, $M_{50}X_{50}PO$, and XPO. The elements in MXPOs form different crystals from CMAS. **h**, **i** Different types of Ap chemical compositions in MPO and (**j**-**k**) chemical compositions of Ap in XPO. The higher content of the framed elements corresponds to a stronger reactive diffusion activity. The schematic diagrams within the dotted lines represent the shape characteristics of the crystal products free in the CMAS. **l** Phase boundary between the interface ceramic and the reaction products. **m** Residual nanocrystals within the dense reaction product layer. **n** A schematic diagram illustrating the influence of the ultra-high-entropy effect on reaction diffusion. (for further detail see Supplementary Note. 7).

orientations (predominantly horizontal) were observed, some adhering closely to the P-rich layer, with dominantly Tb, Dy, Ho, and Er concentrations (Fig. 4j, k).

MXPOs can impede further corrosion by CMAS through the formation of a dense reaction layer. This is attributed to the precipitation of Ap, resulting from the combination of RE^{3+} with Ca and Si from CMAS to form a new phase. Samples containing larger rare earth elements exhibited the thinnest dense reaction layer. This suggests that when M and X ions coexist, an increased proportion of X ions promotes the corrosion reaction.

From a thermodynamic perspective, the incorporation of X ions homogenizes the composition of apatite, identified as the primary degradation-inducing phase across different spatial distributions, and the rare earth content in these phases tends to remain relatively high (Fig. 4g). As a result, generating a unit quantity of reaction products requires a greater supply of rare earth elements. Notably, the performance trend shifts at XPO. From a kinetic perspective, Ap, composed of X elements, exhibits a higher orientation and morphological density, which compensates for the corrosion rate during shorter reaction durations (10 h).

Another critical factor is the impact of the ultra-high-entropy design on the overall corrosion resistance of MXPOs. We observe that increasing the number of cation species leads to a progressive reduction in the thickness of the corrosion product layer. For this purpose, we used $LaPO_4$ as a reference and examined the CMAS corrosion behavior of samples with different entropy levels in terms of both grain-boundary and intragranular stability (Supplementary Fig. 42). (i) Grain-boundary state: in all samples, the grain-boundary interfaces are sharp and smooth, with no evidence of any secondary grain-boundary phases. Furthermore, neither low-entropy nor high-entropy specimens exhibit any wetted CMAS glass at the grain boundaries or at the interfaces between the boundaries and the product grains, indicating that CMAS infiltration into the dense reaction layer is highly impeded (Supplementary Figs. 43, 44). (ii) Intra-granular state: residual ceramic nanocrystals remain embedded within the dense product layer of MXPOs, indicating that, under the same

reaction times, those ceramic matrices are not fully converted-unlike the case for $LaPO_4$ (Fig. 4m and Supplementary Fig. 44). These observations confirm that MXPOs exhibit lower reaction rates and that corrosion products form directly at the ceramic interface rather than via a dissolution–reprecipitation mechanism.

The primary distinction between high-entropy and low-entropy materials lies in the complexity of their compositions. One of the core benefits of high-entropy ceramics is the disordered distribution of multiple cation species: adjacent lattice sites host ions of differing radii, masses, and electronegativities. This deviation from an ideal, periodic lattice generates pronounced local distortions, which in turn elevate the frequency of atomic collisions and scattering.

Although CMAS corrosion is, at its core, a macroscale reaction - namely, the interdiffusion of ceramic and CMAS atoms to form new crystalline phases - these local lattice distortions impose additional diffusion barriers. From the standpoint of diffusive driving forces, lattice distortions create local fluctuations in potential energy. Once an atom migrates into a locally stable, lower-energy site, it must overcome a higher energy barrier to move to the next lattice position[32]. Considering the diffusion process itself, the disorder inherent in high-entropy systems further reduces lattice symmetry. In addition, the theoretical unit-cell density of MXPOs increases compared with certain low-entropy phosphates that contain larger-radius ions (Supplementary Tables 5–7). The resulting compression of interstitial polyhedral sites likely impedes both atomic substitution and vacancy migration (Fig. 4n). The extreme compositional complexity of ultra-high-entropy designs amplifies these effects, thereby slowing the overall reaction rate.

At nearly identical entropy levels, differences in phase and composition directly lead to variations in corrosion behavior. To further determine the mechanistic influence of the M/X ratio on the thermodynamic and kinetic behavior of MXPOs during interaction with CMAS, we calculated the cation binding efficiency with CMAS based on the actual elemental composition of each reaction product (Fig. 5a). The fundamental calculation logic for this parameter is the ratio of the element content originating from the ceramic to that originating from CMAS in the product crystals.

From the final observed trends, the diffusion behavior of P^{5+} ions exhibits no significant variation across different systems in all apatite products. However, among the rare earth elements, the CMAS binding efficiency of M-group elements is higher than that of X-group elements, and this difference becomes more pronounced as the M/X ratio decreases. Despite the increasing proportion of X-group elements, the actual M/X elemental content trend in the P-rich layer has not been reversed, with M elements still being present in large quantities (Fig. 5b).

Therefore, to maintain the stoichiometry of the P-rich products influenced by thermodynamics, CMAS must further extract sufficient M-group elements from the ceramic substrate. This tendency results in an increasing product layer depth in ceramic compositions with lower M-element content, which aligns with the observed phenomena. Notably, we propose that the growth of the P-rich layer originates from a direct transformation of the ceramic substrate, as confirmed by the presence of inherited circular pores from the substrate (Supplementary Fig. 30). In contrast, for the other two types of apatite, the saturation solubility of M and X elements in CMAS plays a more critical role.

We extended the reaction time to explore the evolution of the corrosion behavior (Fig. 5c–e and Supplementary Figs. 31,38,40,41). The thickness trend of the dense product layer in MXPOs remained similar to that observed in short-term reactions. The key difference is that the apatite products of all MXPOs gradually become more consistent as the holding time increases. In addition, their morphological kinetics also exhibit a high degree of uniformity, such as the formation of an additional layer of polygonal apatite attached to the P-rich product. Compositional analysis of the three types of products revealed that the diffusion trends of P ions and rare earth ions were opposite - apatite located farther from the interface contained a higher concentration of rare earth elements (Fig. 5d). Notably, the continuous double-layer structure at the XPO-CMAS interface disappeared, leading to a deeper P-rich layer. However, its overall behavior remained comparable to that of other single-phase MXPOs.

Combining the results of the different reaction times, the difference in CMAS interaction behaviors exhibited by MXPOs with different phase states lies in the thermodynamic diffusion tendencies of rare earth ions and the kinetic morphologies of the product crystals. Specifically, M ions have a stronger tendency to form apatite products, which means that even MXPOs with low M content can contribute a significant number of ions to the product layer. Furthermore, the kinetic morphology of the product crystals - primarily the Ap that adheres to the interface - plays an auxiliary barrier role, significantly reducing the probability of contact between the melt and the dense layer. However, this mechanism becomes unstable as the reaction progresses.

Corrosion behavior of MXPOs with natural sand

Based on the reaction mechanisms of CMAS and MXPOs discussed in the previous section, calcium plays a crucial role in both the sample and the melt. In natural environments, sediment composition varies considerably based on protolith and deposition environment. This raises the question: if the calcium content in CMAS is lower, can it be insufficient to stabilize the protective dense layer? To explore this aspect further, we selected natural sand with a “melting temperature”[41] similar to that of CMAS but possessing a lower Ca/Si ratio (Fig. 6a–e and Supplementary Figs. 24, 25). This enabled us to investigate the reaction mechanism in greater depth.

To investigate the intrinsic properties of the sand, we quantified the evolution of the morphology of sand cylinders with temperature through melting in terms of characteristic “temperatures” (original, shrinkage, deformation, hemisphere, flow) as the sand melts and spreads (Fig. 6c and Supplementary Notes. 7). The results indicate that (1) the initial sintering of the sand (ST) is drastically postponed by the requirement of melting the crystalline initial state and 2) the final flow temperature (FT) of the sand is also delayed to higher temperature due to the compositional difference (i.e., higher SiO_2 content). We note, however, that their hemisphere temperatures (HT) are similar. These results highlight the challenge of representing natural sand via CMAS analog.

After thermal treatment (1300 °C, 10 h), the morphology of the corrosion interface between MXPOs and sand exhibits an only slightly different behavior from that of CMAS (Fig. 6f and Supplementary Figs. 32–36). Firstly, all MXPOs formed a dense phosphorus-rich layer, indicating that the phosphorus-dominated protective mechanism persists even under low calcium conditions. Secondly, the outer layer products displayed a distinct ‘frost flower’ distribution, with the distribution of the Ap crystals shifting from aggregated to dispersed (Supplementary Fig. 37). Furthermore, we observed an anomalous phenomenon: the emergence of a bilayer structure (Ap + P dense layer) in the corrosion zone following the dynamic spreading of the melt (Fig. 6f and Supplementary Fig. 33). This protective mechanism effectively isolates CMAS, resulting in an extremely low corrosion depth.

Grain boundary penetration in multiphase samples became more pronounced in the higher SiO_2 (sand) environment. Several Si-rich glass domains were interspersed within the ceramic layer near the reaction interface, and no Ap crystallization was observed. From the perspective of grain stability, the multiphase sample can be regarded as a mixture of single-phase M and single-phase X structures. Although their diffusion tendencies in the CMAS melt are different, the thermodynamics of the reaction products are not significantly different

https://doi.org/10.1038/s41467-025-64481-0

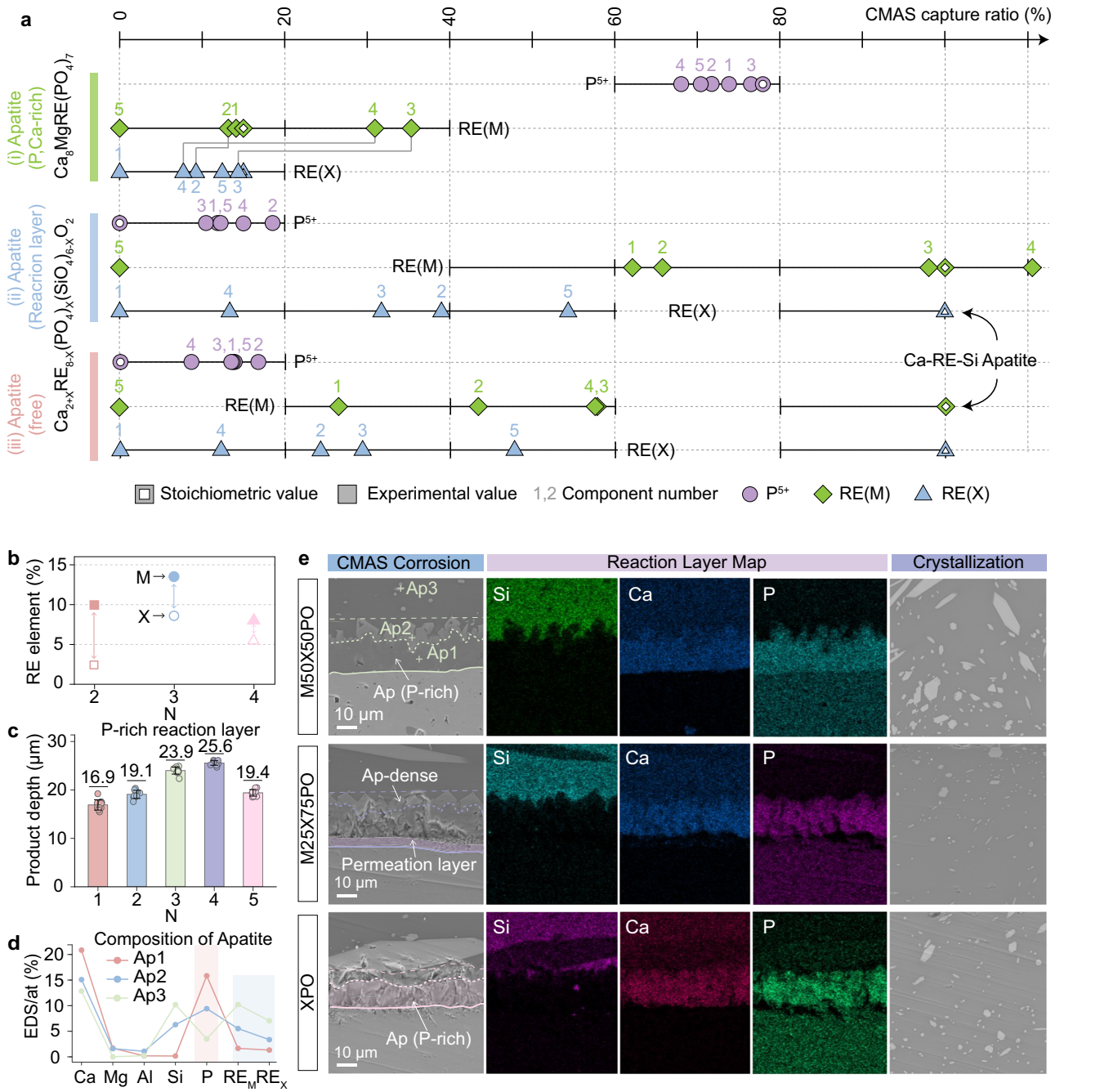

Fig. 5 | Cation diffusion propensity based on CMAS capture capacity measures and the effect of extended reaction time on interaction behavior. a CMAS capture ratio of cations corresponding to the three types of apatite, classified based on the spatial distribution of product formation. A higher value indicates a lower efficiency of the element in binding CMAS per unit quantity. **b** Actual proportion of M group and X group elements in the phosphorus-rich crystals formed after the reaction of MXPOs containing both M and X elements with CMAS. **c** Depth of the phosphorus-rich dense layer product formed at the MXPOs-CMAS interface after extending the reaction time to 50 h. The number on the line is the average value of thickness. **d** The composition of the apatite product at the MXPOs-CMAS reaction interface. The shaded area highlights the content from phosphate cations. **e** $M_{75}X_{25}PO$, $M_{25}X_{75}PO$, and XPO-CMAS reaction interface morphology.

from those of the single-phase MXPOs. From the viewpoint of the grain boundary environment, some of the grain boundaries in the multi-phase sample are replaced by M-X phase boundaries (Supplementary Fig. 39). Due to the significant difference in crystal symmetry between the M and X phases, these interfaces are more likely to be incoherent, exhibiting high interface energy and low thermodynamic stability[42,43]. This relatively unstable interface provides a preferential pathway for the infiltration and corrosion of the CMAS melt[44].

As the M/X ratio gradually decreased, the XPO exhibited the thinnest corrosion depth (Fig. 6g). Moreover, after high-temperature melting and cooling, the CMAS glass at the center detached entirely, leaving only thin remnants at the edges. Notably, the detachment of the glass removed the reaction layer, revealing an intact ceramic surface. Furthermore, we discovered numerous transversely aligned cracks at the junction between the residual glass and the ceramic. These cracks likely originated during the rapid cooling phase following corrosion, where stress mismatch led to partial exfoliation of the glass along with the reaction layer.

These findings demonstrate that in interactions with natural sand, single-phase MXPOs exhibit superior corrosion resistance, whereas

https://doi.org/10.1038/s41467-025-64481-0

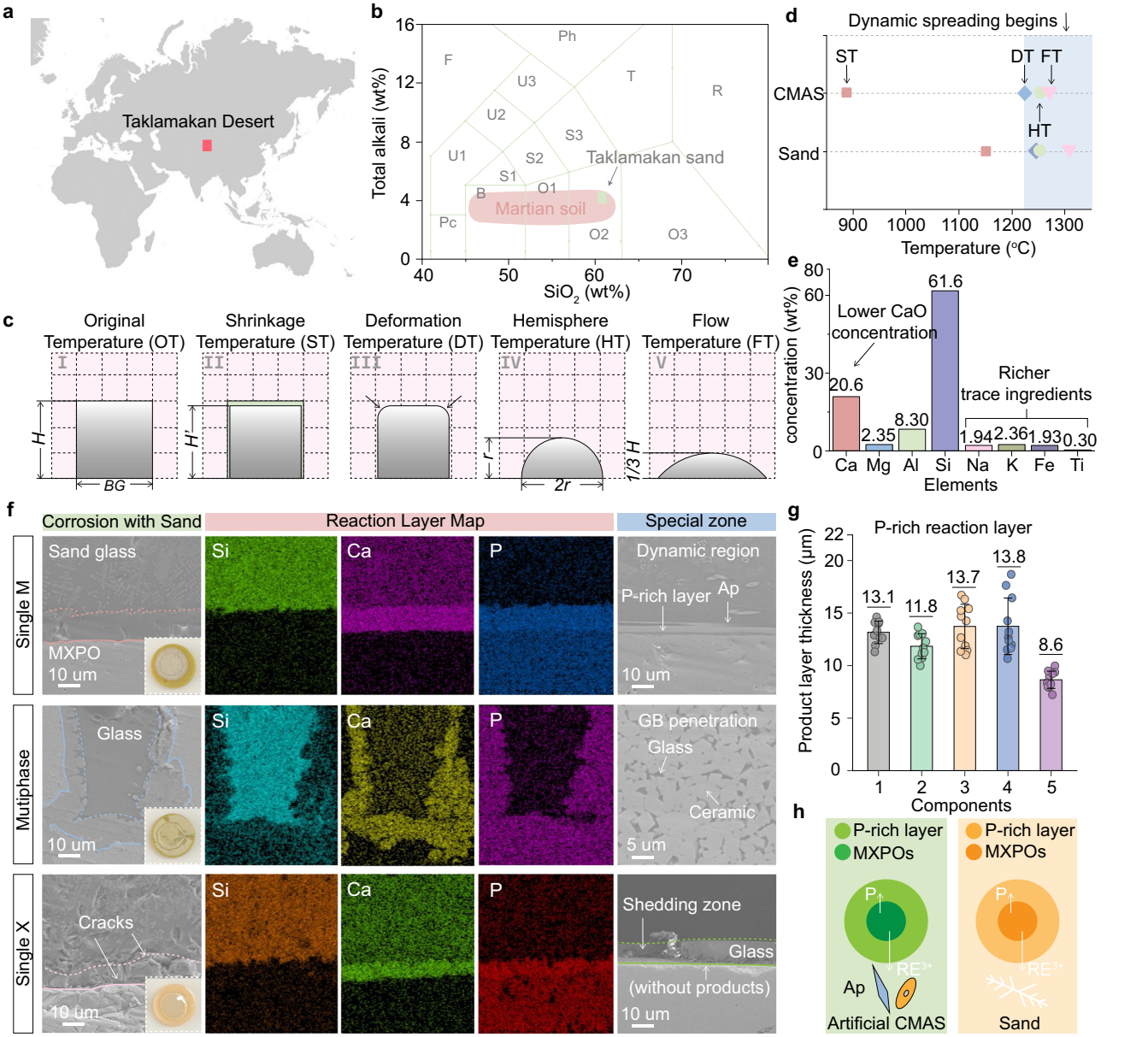

Fig. 6 | High-temperature reaction behavior of MXPOs with sand. a, b Sampling locations for natural sand and total alkalinity factor. Such factors can help to delineate mineral species. The red areas represent the distribution of Martian soils[23,51,52]. **c, d** quantification of the nodes of the CMAS melting process and the melting temperatures of the two CMAS. Artificial CMAS is easy to sinter at low temperatures, and the melting interval is similar to that of sand. **e** chemical composition of Sand. **f, g** $M_{75}X_{25}PO$, $M_{50}X_{50}PO$, and XPO-Sand reaction interface morphology and penetration depth. The number on the line is the average value of thickness. The inset figures represent the top morphology of the MXPOs ceramic after being loaded with sand and corroded. **h** Distribution of different product morphologies at the interface after different CMAS reactions.

multiphase samples produce thicker corrosion products and show more pronounced grain boundary penetration. The reduction in the Ca/Si ratio does not significantly affect phosphorus's ability to capture calcium, thereby maintaining the thermodynamic logic of the defensive mechanism. Nevertheless, in contrast to the behavior observed in artificial CMAS, the precipitation of RE^{3+} becomes more dispersed.

Corrosion behavior of Sand-MXPOs under different atmospheres

In current and future space exploration scenarios, particulates present on surfaces and in the atmosphere pose significant corrosion risks to infrastructure[45]. As an example, dust that melts under high-temperature airflow during spacecraft launch and landing can corrode both the flight structure and the launch/landing platform[46]. In addition, in situ resource utilization (ISRU) operations in surface construction projects, which involve heating regolith to extract resources, require processing equipment that can resist melt corrosion[47,48]. Another challenge is that spacecraft entering or exiting the atmosphere are subjected to extreme temperatures that can rapidly melt suspended dust, leading to degradation of protective structures and certain connecting components[4].

In the expansive field of space exploration, Mars and the Moon have consistently been primary targets for human investigation. One of the most apparent distinctions between these celestial bodies and Earth lies in their surface environments, their oxidation states, and their atmospheres. For this reason, we have also observed the melting and spreading processes of natural sand on MXPOs under CO_2 atmosphere and vacuum conditions (Fig. 7a, b).

https://doi.org/10.1038/s41467-025-64481-0

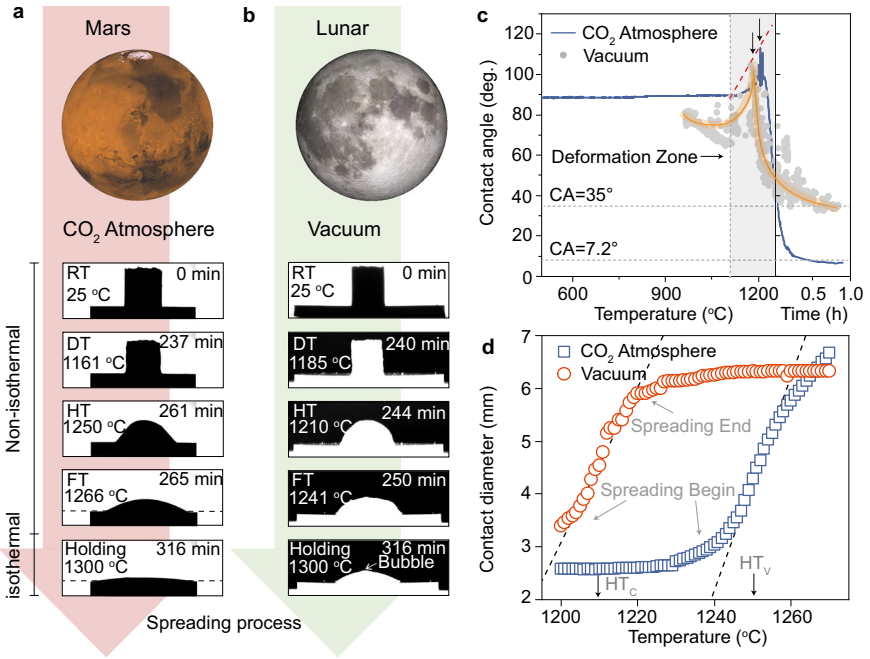

Fig. 7 | Sand spreading tests under CO_2 and vacuum atmospheres. a, **b** Melt diffusion processes in sand powder columns under different atmospheres. CO_2 and vacuum correspond to the main gaseous environments of Mars and the Moon, respectively[53–55]. Sand dynamic melting under vacuum starts much earlier. **c** Curves of the contact angle of the powder columns with the spreading process. The yellow curve is a discrete trending of the data due to bubble bursting under vacuum. The gray shadow indicates the temperature range that the sand in a vacuum undergoes from the beginning of melting to the end of heating. The gray shading indicates the temperature range experienced by the sand under vacuum from the onset of melting to the end of heating. The black arrows mark the inflection points of the wetting contact angle in both atmospheres, each followed by rapid spreading. The red dashed line connects these inflection points to highlight the delayed spreading of sand in the CO_2 atmosphere. **d** Trend of the contact line between molten Sand and MXPOs is used to quantify the rate of spreading.

For MPO (which exhibits the most stable resistance to CMAS corrosion), the spreading process of sand under different atmospheric conditions reveals marked differences. In terms of the spreading dynamics, *in vacuo*, CMAS appears to begin melting earlier, causing an earlier start of the decreasing of the contact angle (Fig. 7c). This phenomenon may be attributed to the melting kinetics under different atmospheric pressures. Regarding the spreading rate (Fig. 7d), CMAS under vacuum conditions demonstrates a trend of initial slow progression followed by acceleration, which differs from the continuous spreading observed under CO_2 conditions.

From these results, it is evident that the spreading of CMAS under vacuum conditions is less complete, with its final contact angle significantly larger than that observed in a CO_2 atmosphere. This phenomenon has two implications in terms of corrosion risk. Firstly, a smaller contact area suggests a reduced area of damage. However, this is accompanied by continuous penetration of CMAS. Secondly, while a greater degree of spreading increases the area exposed to corrosion, the smaller amount of CMAS per unit area may allow protective mechanisms to function more effectively, potentially leading to an earlier termination of the reaction.

In summary, we explored the structural transitions and high-temperature CMAS corrosion behavior of a series of ultra-high entropy phosphates based on rare earth element gradient design. The reduction in the M/X element ratio caused the solid solution to gradually transition from a single monazite phase to a single xenotime phase. Regardless of composition and structural transitions, all samples maintained high density and excellent high-temperature phase stability. Furthermore, the differences in the CMAS interaction behavior exhibited by MXPOs with different phases are reflected in the thermodynamic diffusion tendencies of the rare earth ions and the kinetic morphology of the product crystals. M-group elements with larger radii appear to exhibit more stable corrosion resistance. Thermodynamically, they are more inclined to capture Ca in conjunction with P to form a dense protective layer. Kinetically, under certain conditions, the apatite phase that adheres tightly to the interface serves as an auxiliary barrier, thereby increasing the difficulty for the melt to continue its erosion. Our gradient design of compositions demonstrated the reaction tendencies of all rare earth elements with CMAS and identified outstanding corrosion-resistant single-phase compositions. The substantially reduced reaction rates achieved through an ultra-high-entropy design, combined with a more flexible elemental palette, establish a new paradigm and theoretical framework for overcoming phosphate design limitations and improving corrosion resistance. The outlook for planetary applications contains further subtleties.

Method

Sample preparation

Five groups of MXPOs samples with complex compositions and ultra-high entropy values were prepared using the coprecipitation method (Detailed information in Supplementary Note. 1 and Supplementary Figs. 1–4). Lanthanide rare earth (La to Lu, and Y) hydrated nitrates were used as the rare earth sources, and diammonium hydrogen phosphate was used as the precipitating agent. Note that the ratio of total rare earth nitrates to $(NH_4)_2HPO_4$ should be less than 1:1.3 to ensure complete precipitation. After mixing, the solid-liquid mixture was fully reacted by stirring at room temperature for at least 12 h. Subsequently, the mixture was separated by centrifugation, and the solid product was washed repeatedly with deionized water and ethanol at least 3 times until the pH of the supernatant was neutral. After drying at atmospheric pressure, the powder agglomerated into blocks. It was then ground using an agate grinder to a particle size below 200 μm. Subsequently, the powder was further milled in anhydrous ethanol using zirconia balls as the medium at a rotation speed of 350 $r \cdot min^{-1}$. Finally, the powder was passed through a 300-mesh sieve. Polyvinyl alcohol (PVA) solution was then added as a binder for spherical

granulation, resulting in a powder with good flowability, high particle roundness, and continuous particle size distribution.

High-temperature properties tests

Three methods were used to test the high-temperature stability of the samples for different temperature bands (Supplementary Fig. 20). In situ ascent XRD was used to test for changes in the crystal structure of samples from room temperature to 1200 °C. The heating rate for this test was 10 °C per minute. Upon reaching the target temperature, the sample was held for 15 min before diffraction data were collected, with data acquired at 50 °C intervals. Differential scanning calorimetry was used to monitor real-time mass changes and heat exchange of the sample powder, with data collected at a heating rate of 10 °C per minute. Finally, rapid thermal vibration experiments were performed at >1500 °C using a flash heating furnace to examine macro-micro stability under extreme conditions. Here, the high-temperature thermal vibration treatment of the samples was carried out in three sets of 10 pulses each, with a constant temperature time of 10 s and a maximum temperature of about 2000 °C. A laser thermal conductivity instrument was used to measure the specific heat capacity and thermal diffusivity of bulk samples (with a diameter of 12.6 mm), heating at a rate of 10 °C·min^{-1} with measurement intervals of 100 °C. By combining the actual density of the sample, the corresponding thermal conductivity at a certain temperature can be calculated.

CMAS corrosion tests

Two types of CMAS including synthetic CMAS and naturally collected CMAS (Sand) were used in this work. The CMAS powder was weighed and pressed into a 3 mm diameter cylindrical mold, compacted, and placed in the center of the polished ceramic surface at a loading of ~140 mg·cm^{-2}. Subsequently, the assemblies were placed in a muffle furnace at 1300 °C for 10 h for chemical corrosion tests. On the other hand, the assemblies were placed in a high-temperature furnace equipped with an optical camera for real-time acquisition of the CMAS physical spreading state.

Structure and morphology characterization

Powder X-ray diffraction (XRD) patterns were recorded on a Bruker Advanced D8 diffractometer using Cu-Kα radiation (λ = 1.54056 Å). A scanning electron microscope (SEM, Sigma 300 Zeiss) and transmission electron microscope (TEM, Thermo-Fisher Scientific) equipped with an energy-dispersive X-ray spectrometer (EDS, Oxford Instruments) was used to characterize the microscopic morphology, elemental composition. For cross-sectional observations, it was also necessary to mechanically grind and polish the samples to 0.25 μm. The depth of corrosion was identified by the lining of the reaction product layer under SEM and was derived from the average of the data at each location. Raman spectroscopy (Raman, DXR, Thermo Scientific) determines the nature of ionic bonding by detecting vibrational bands, and X-ray photoelectron spectroscopy (XPS, K-Alpha, Thermo Scientific) is able to characterize the valence state of each element.

Ethics & inclusion statement

The authors affirm that all contributions were made in accordance with globally recognized ethical standards and inclusion principles. They further declare that this study does not involve any potential risks to human subjects, animals, or the environment, and that all research activities were conducted with full adherence to ethical guidelines.

Data availability

All relevant data that support the findings are available within this article and supplementary information, and are also available from the authors upon request. Source data are available. Source data are provided in this paper.

References

1. Padture, N. P. Advanced structural ceramics in aerospace propulsion. *Nat. Mater.* **15**, 804–809 (2016).
2. Guo, J. et al. Hypocrystalline ceramic aerogels for thermal insulation at extreme conditions. *Nature* **606**, 909–916 (2022).
3. Zhang, J. et al. Plastic deformation in silicon nitride ceramics via bond switching at coherent interfaces. *Science* **378**, 371–376 (2022).
4. Eswarappa Prameela, S. et al. Materials for extreme environments. *Nat. Rev. Mater.* **8**, 81–88 (2022).
5. Padture, N. P., Gell, M. & Jordan, E. H. Thermal barrier coatings for gas-turbine engine applications. *Science* **296**, 280–284 (2002).
6. Clarke, D. R., Oechsner, M. & Padture, N. P. Thermal-barrier coatings for more efficient gas-turbine engines. *MRS Bull.* **37**, 891–898 (2012).
7. Nicholls, J. Advances in coating design for high-performance gas turbines. *MRS Bull.* **28**, 659–670 (2003).
8. Rashid, A. B., Haque, M., Islam, S. M. M., Uddin Labib, K. M. R. & Chowdhury, P. Breaking boundaries with ceramic matrix composites: A comprehensive overview of materials, manufacturing techniques, transformative applications, recent advancements, and future prospects. *Adv. Mater. Sci. Eng.* **2024**, 1–33 (2024).
9. Ma, X. et al. Design, modeling, and manufacturing of high strain composites for space deployable structures. *Commun. Eng.* **3**, 78 (2024).
10. Knipe, K. et al. Strain response of thermal barrier coatings captured under extreme engine environments through synchrotron X-ray diffraction. *Nat. Commun.* **5**, 4559 (2014).
11. Burger, B. et al. A mobile robotic chemist. *Nature* **583**, 237–241 (2020).
12. Noh, J. An integrated high-throughput robotic platform and active learning approach for accelerated discovery of optimal electrolyte formulations. *Nat. Commun.* **15**, 2757 (2024).
13. Rao, Z. et al. Machine learning–enabled high-entropy alloy discovery. *Science* **378**, 78–85 (2022).
14. Li, W. et al. Generative learning facilitated discovery of high-entropy ceramic dielectrics for capacitive energy storage. *Nat. Commun.* **15**, 4940 (2024).
15. Padture, N. P. Environmental degradation of high-temperature protective coatings for ceramic-matrix composites in gas-turbine engines. *Npj Mater. Degrad.* **3**, 11 (2019).
16. Nieto, A. et al. Calcia–magnesia–alumina–silicate (CMAS) attack mechanisms and roadmap towards Sandphobic thermal and environmental barrier coatings. *Int. Mater. Rev.* **66**, 451–492 (2021).
17. Krämer, S., Yang, J., Levi, C. G. & Johnson, C. A. Thermochemical interaction of thermal barrier coatings with molten CaO–MgO–Al_2O_3 –SiO_2 (CMAS) deposits. *J. Am. Ceram. Soc.* **89**, 3167–3175 (2006).
18. Ericks, A. R., Zok, F. W., Poerschke, D. L. & Levi, C. G. Protocol for selecting exemplary silicate deposit compositions for evaluating thermal and environmental barrier coatings. *J. Am. Ceram. Soc.* **105**, 3665–3688 (2022).
19. Levi, C. G., Hutchinson, J. W., Vidal-Sétif, M.-H. & Johnson, C. A. Environmental degradation of thermal-barrier coatings by molten deposits. *MRS Bull.* **37**, 932–941 (2012).
20. Drexler, J. M., Ortiz, A. L. & Padture, N. P. Composition effects of thermal barrier coating ceramics on their interaction with molten Ca–Mg–Al–silicate (CMAS) glass. *Acta Mater.* **60**, 5437–5447 (2012).
21. Song, W. et al. Impact interaction of in-flight high-energy molten volcanic ash droplets with jet engines. *Acta Mater.* **171**, 119–131 (2019).
22. Li, C. et al. Characteristics of the lunar samples returned by the Chang'E-5 mission. *Natl Sci. Rev.* **9**, nwab188 (2022).
23. Achilles, C. N. et al. Mineralogy of an active eolian sediment from the Namib dune, Gale crater, Mars. *J. Geophys. Res. Planets* **122**, 2344–2361 (2017).

24. Song, W. et al. Biomimetic super "Silicate" phobicity and superhydrophobicity of ceramic material. *Adv. Mater. Interfaces* **9**, 2201267 (2022).
25. Cheng, F. et al. Fluorite-pyrochlore structured high-entropy oxides: Tuning the ratio of B-site cations for resistance to CMAS corrosion. *Corros. Sci.* **218**, 111199 (2023).
26. Chen, Z. et al. Medium-entropy monosilicates deliver high corrosion resistance to calcium-magnesium aluminosilicate molten salt. *Adv. Sci.* **11**, 2400736 (2024).
27. Guo, L. et al. Yb doping effects on CMAS corrosion resistance of Yb-doped $GdPO_4$ by first-principles calculation and experimental investigation. *Corros. Sci.* **218**, 111175 (2023).
28. Han, J., Wang, Y., Liu, R. & Wan, F. Theoretical and experimental investigation of Xenotime-type rare earth phosphate REPO4, (RE = Lu, Yb, Er, Y and Sc) for potential environmental barrier coating applications. *Sci. Rep.* **10**, 13681 (2020).
29. Li, W. et al. Phase structure evolution and chemical durability studies of $Gd_{1-x}Yb_xPO_4$ ceramics for immobilization of minor actinides. *J. Mater. Sci.* **53**, 6366–6377 (2018).
30. Cheng, F. et al. Ti^{4+}-incorporated fluorite-structured high-entropy oxide (Ce,Hf,Y,Pr,Gd)$O_{2-\delta}$: Optimizing preparation and CMAS corrosion behavior. *J. Adv. Ceram.* **11**, 1801–1814 (2022).
31. Luo, Y. et al. Phase formation capability and compositional design of β-phase multiple rare-earth principal component disilicates. *Nat. Commun.* **14**, 1275 (2023).
32. Hsu, W.-L., Tsai, C.-W., Yeh, A.-C. & Yeh, J.-W. Clarifying the four core effects of high-entropy materials. *Nat. Rev. Chem.* **8**, 471–485 (2024).
33. Siegel, R. & M. Spuckler, C. Analysis of thermal radiation effects on temperatures in turbine engine thermal barrier coatings. *Mater. Sci. Eng. A* **245**, 150–159 (1998).
34. Wright, A. J. et al. Short-range order and origin of the low thermal conductivity in compositionally complex rare-earth niobates and tantalates. *Acta Mater.* **235**, 118056 (2022).
35. Su, L. et al. Direct observation of elemental fluctuation and oxygen octahedral distortion-dependent charge distribution in high entropy oxides. *Nat. Commun.* **13**, 2358 (2022).
36. Oses, C., Toher, C. & Curtarolo, S. High-entropy ceramics. *Nat. Rev. Mater.* **5**, 295–309 (2020).
37. Wan, C. L. et al. Effect of point defects on the thermal transport properties of $(La_xGd_{1-x})_2Zr_2O_7$: Experiment and theoretical model. *Phys. Rev. B* **74**, 144109 (2006).
38. Guo, L., Feng, J. & Meng, S. Corrosion resistance of GdPO4 thermal barrier coating candidate in the presence of CMAS + NaVO3 and CMAS. *Corros. Sci.* **208**, 110628 (2022).
39. Dong, H. et al. CMAS corrosion behavior of a $LaPO_4$ ceramic prepared by spark plasma sintering. *J. Am. Ceram. Soc.* **106**, 5420–5430 (2023).
40. Bryce, K., Shih, Y.-T., Huang, L. & Lian, J. Calcium-Magnesium-Aluminosilicate (CMAS) corrosion resistance of high entropy rare-earth phosphate $(Lu_{0.2}Yb_{0.2}Er_{0.2}Y_{0.2}Gd_{0.2})PO_4$: A novel environmental barrier coating candidate. *J. Eur. Ceram. Soc.* **43**, 6461–6472 (2023).
41. Song, W. et al. Volcanic ash melting under conditions relevant to ash turbine interactions. *Nat. Commun.* **7**, 10795 (2016).
42. Rohrer, G. S. Grain boundary energy anisotropy: a review. *J. Mater. Sci.* **46**, 5881–5895 (2011).
43. Watanabe, T. Grain boundary engineering: historical perspective and future prospects. *J. Mater. Sci.* **46**, 4095–4115 (2011).
44. Aaron, H. B. & Weinberg, F. Preferential diffusion along interphase boundaries. *Acta Met.* **20**, 339–344 (1972).
45. Zakharov, A. V., Zelenyi, L. M. & Popel, S. I. Lunar dust: Properties and potential hazards. *Sol. Syst. Res.* **54**, 455–476 (2020).
46. Li, X., Gao, Y., Zhou, Y., Han, W. & Zhou, C. A review on design and construction of the lunar launch/landing infrastructure. *Adv. Space Res.* **74**, 4030–4049 (2024).
47. Farries, K. W., Visintin, P., Smith, S. T. & Van Eyk, P. Sintered or melted regolith for lunar construction: state-of-the-art review and future research directions. *Constr. Build. Mater.* **296**, 123627 (2021).
48. Palos, M. F., Serra, P., Fereres, S., Stephenson, K. & González-Cinca, R. Lunar ISRU energy storage and electricity generation. *Acta Astronaut.* **170**, 412–420 (2020).
49. Heuser, J. M. et al. Structural characterization of (Sm,Tb)PO_4 solid solutions and pressure-induced phase transitions. *J. Eur. Ceram. Soc.* **38**, 4070–4081 (2018).
50. Hay, R. S., Boakye, E. E. & Mogilevsky, P. Transformation plasticity in $TbPO_4$ and (Gd,Dy)PO_4 orthophosphates during indentation of polycrystalline specimens. *J. Eur. Ceram. Soc.* **34**, 773–781 (2014).
51. The Omega Team et al. Phyllosilicates on Mars and implications for early martian climate. *Nature* **438**, 623–627 (2005).
52. Nussinov, M. D., Chernyak, Y. B. & Ettinger, J. L. Model of the fine-grain component of martian soil based on Viking lander data. *Nature* **274**, 859–861 (1978).
53. Kahn, R. The evolution of CO_2 on Mars. *Icarus* **62**, 175–190 (1985).
54. Tomkinson, T., Lee, M. R., Mark, D. F. & Smith, C. L. Sequestration of martian CO_2 by mineral carbonation. *Nat. Commun.* **4**, 2662 (2013).
55. Nie, N. X., Dauphas, N., Zhang, Z. J., Hopp, T. & Sarantos, M. Lunar soil record of atmosphere loss over eons. *Sci. Adv.* **10**, eadm7074 (2024).

Acknowledgements

We are grateful to Wei Wang for providing an artificial CMAS sample, to Zhe Wang for equipment details, Changli Fu for the methods on sample preparation. We thank Tong Liu, Chengyang Jiang, Zhanpeng Chen, and Shankun Wang for vivid discussions and fruitful insights. W.S. also acknowledges the support from the Key R&D Program of Zhejiang (2024SSYS0080), the National Natural Science Foundation of China (52571061) and the Zhejiang Provincial Natural Science Foundation of China (LZ23E010003). D.B.D. acknowledges the support of ERC 2018 ADV Grant 834225 (EAVESDROP).

Author contributions

F.C. conceptualized the original idea, produced and processed the data; W.S., F.C., and D.B.D. advised on the experimental program and assisted in the interpretation of the results. F.C. wrote the manuscript with input from the other authors. Funding for this work was provided primarily by W.S. The final manuscript was reviewed and approved by all coauthors.

Competing interests

The authors declare no competing interests.

Additional information

Supplementary information The online version contains supplementary material available at https://doi.org/10.1038/s41467-025-64481-0.

Correspondence and requests for materials should be addressed to Wenjia Song.

Peer review information *Nature Communications* thanks the anonymous reviewers for their contribution to the peer review of this work. A peer review file is available.